Variations on Nickel Complexes of the *vic*-Dioximes: An Understanding of Factors Affecting Volatility toward Improved Precursors for Metal−Organic Chemical Vapor Deposition of Nickel

James D. Martin,[†] Philip Hogan,[†] Khalil A. Abboud,[‡] and
Klaus-Hermann Dahmen*,[†]

*The Department of Chemistry and MARTECH, The Florida State University,
Tallahassee, Florida 32306, and The Department of Chemistry, The University of Florida,
Gainesville, Florida 32611*

The *vic*-dioxime complexes bis(2,3-butanedionedioximato)nickel(II), Ni(dmg)$_2$; bis(3,4-hexanedionedioximato)nickel(II), Ni(deg)$_2$; bis(4,5-octanedionedioximato)nickel(II), Ni(dpg)$_2$; bis(ethanedialdioximato)nickel(II), Ni(g)$_2$; bis(1,2-diphenylethanedionedioximato)nickel(II), Ni(dbg)$_2$; bis(1,2-cyclohexanedionedioximato)nickel(II), Ni(nox)$_2$; and bis(2,3-pentanedionedioximato)nickel(II), Ni(meg)$_2$, were prepared. Their volatilities were compared under ambient and reduced pressure using thermogravimetry. Ni(deg)$_2$ and Ni(dpg)$_2$ were the most volatile, and the variation in volatility of each complex was explained on the basis of ligand effects, crystal packing, and nickel−nickel distances using solid-state electronic spectra. The crystal structure of Ni(dpg)$_2$ was determined for the first time: monoclinic crystal system, *C*2/*c* space group. The complex packs in pairs related by the *c*-glide plane symmetry. Short intrapair distances of 3.312(2) Å are observed between Ni and N with short and long Ni−Ni distances of 3.2044(5) and 5.7964(5) Å, respectively. Metal−organic chemical vapor deposition (MOCVD) experiments were conducted using Ni(deg)$_2$ as precursor in a vertical cold-walled reactor. The precursor transport and film growth behavior, morphology, and composition have been examined. Pure films could be grown between 350 and 400 °C in helium. Growth rates were greater with additional hydrogen, but the films were heavily contaminated with carbon. The difference in growth rates and film morphology for the different reactor conditions was investigated.

Introduction

Nickel finds a place in a variety of thin film materials, often alloyed with other elements. As a contact material in semiconductor devices, AuGeNi alloys have been extensively used because of their ability, low contact resistance, and good reproducibility.[1] NiP$_2$ is valued in InP-based semiconductors because it grows epitaxially, giving stability and low resistance as an interconnect.[2] Nickel silicides, gallides, and aluminides also have potential use in these applications.[3−5] Other thin film forms requiring nickel include nanostructured magnetic materials,[6−9] hydrogen storage alloys,[10−13] and micro-mechanical actuators.[14] The suitability of metal−organic chemical vapor deposition (MOCVD) as a technique for preparing such complex materials rests in the availability of a variety of precursors, each with their own properties, conditions, and reactivities by which they will give a film. For a compound to be used as a precursor in MOCVD, it must be volatile and transportable in the gas phase, thermally stable at the evaporation temperature, and decomposable at the substrate temperature. Ideally the precursor should also be air-stable, nontoxic, and cheap. Precursors that have been used for nickel deposition include the very toxic nickel tetracarbonyl,[15,16] and the nickelocenes Ni(η^5-C$_5$H$_5$)$_2$[17]

* To whom correspondence should be addressed.
† The Florida State University.
‡ The University of Florida.

(1) Braslau, N.; Gunn, J.; Staples, J. *Solid State Electron.* **1967**, *10*, 381.
(2) Murarka, S. *Metallization: Theory & Practice for VLSI & ULSI*; Butterworth: Heinemann, 1993.
(3) Dormans, G. *J. Crystal Growth* **1991**, *108*, 806.
(4) Kaesz, H. D.; Williams, R. S.; Hicks, R. F.; Zink, J. I.; Chen, Y. J.; Müller, H. J.; Xue, Z.; Xu, D.; Shuh, D. K.; Kim, Y. K. *New. J. Chem.* **1990**, *14*, 527.
(5) Fraser, B.; Brandt, L.; Stovall, W. K.; Kaesz, H. D.; Khan, S. I.; Maury, F. *J. Organomet. Chem.* **1994**, *472*, 317.
(6) Watson, M.; Banard, J.; Hossain, S.; Parker, M. *J. Appl. Phys.* **1993**, *73*, 5506.
(7) Kitada, M.; Yamamoto, K.; Shimizu, N. *J. Magn. Magn. Mater.* **1993**, *124*, 243.
(8) Atzmony, U.; Swartzendruber, L.; Bennet, L.; Dariel, M.; Lashmore, D.; Rubinstein, M.; Lubitz, P. *J. Magn. Magn. Mater.* **1987**, *69*, 237.
(9) Al-Kassab, T.; Macht, M.; Naundorf, V.; Wollenberger, H.; Chambreland, S.; Danoix, F.; Blavette, D. *Appl. Surf. Sci.* **1996**, *94/95*, 306.
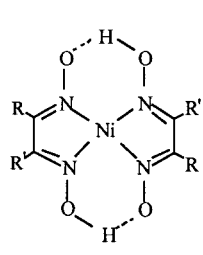(10) Willems, J. *Phillips J. Res. Suppl. 1* **1987**, *39*, 1.
(11) Kuriyama, N.; Sakai, T.; Miyamura, H.; Tanaka, H.; Ishikawa, H.; Uehara, I. *Vacuum* **1996**, *47*, 889.
(12) Adachi, G.; Sakaguchi, H.; Niki, K.; Nagai, N.; Shitnokawa, J. *J. Less-Common Met.* **1985**, *108*, 101.
(13) Sakai, T.; Ishikawa, H.; Myamura, H.; Kuriyama, N. *J. Electrochem. Soc.* **1991**, *138*, 4.
(14) Goldberg, F.; Knystautas, E. *Mat. Sci. Eng.* **1996**, *B40*, 185.
(15) Mond, L. *J. Chem. Soc.* **1885**, 945.

| R	R'	Symbol	Name
CH_3	CH_3	Ni(dmg)$_2$	Bis(2,3-butanedionedioximato)nickel(II)
C_2H_5	C_2H_5	Ni(deg)$_2$	Bis(3,4-hexanedionedioximato)nickel(II)
C_3H_7	C_3H_7	Ni(dpg)$_2$	Bis(4,5-octanedionedioximato)nickel(II)
C_6H_5	C_6H_5	Ni(dbg)$_2$	Bis(1,2-diphenylethanedionedioximato)nickel(II)
CH_3	C_2H_5	Ni(meg)$_2$	Bis(2,3-pentanedionedioximato)nickel(II)
H	H	Ni(g)$_2$	Bis(ethanedialdioximato)nickel(II)
-CH_2CH_2-	-CH_2CH_2-	Ni(nox)$_2$	Bis(1,2-cyclohexanedionedioximato)nickel(II)

Figure 1. *Vic*-dioximes of nickel synthesized for this study.

and Ni(η^5-$CH_3C_5H_4$)$_2$.[18] The β-diketonates, nickel acetylacetone,[19] and nickel hexafluoroacetylacetone[20] also reportedly give nickel films. Because the quality of metal films often suffers from incorporation of impurities such as oxygen or carbon from the ligand[21] and the difficulties encountered in using β-diketonates for nickel films, we turned to the nitrogen-bonded ligand system of the *vic*-dioximes. This system has been known for years for its use in quantitative analysis and modeling vitamin B12[22] and has been studied for its semiconducting properties.[23] The utilization of its complex chemistry in chemical vapor deposition has only recently been demonstrated. In our previous works,[24,25] we used bis-(2,3-butanedionedioximato)nickel(II), Ni(dmg)$_2$, to grow nickel films. This precursor gave the best films at a substrate temperature of 540 °C. The vaporization temperature used was 240 °C at 4 mbar total pressure, and hydrogen was necessary to produce films.

It was the goal of this present work to vary the R groups on the ligand, producing varied and potentially improved precursors (Figure 1). Following thermogravimetric analysis (TGA), differential thermal analysis (DTA), and UV/vis spectroscopy, MOCVD was carried out on the most promising complexes.

Experimental Section

Synthesis. Except for 2,3-butanedionedioxime (dimethylglyoxime) and 1,2-cyclohexanedionedioxime, which were purchased from Aldrich, all the other ligands were synthesized from the corresponding α-diketones by stirring overnight with an excess of hydroxylamine in aqueous solution.[26] The resulting mixtures were rotovapped to one-quarter of their initial volume, cooled, filtered, washed with cold water, and dried under vacuum. The products were confirmed by IR and ^{1}H NMR, with yields ranging from 45 to 60%. With the exception of 4,5-octanedione, all the α-diketones were purchased from Aldrich and used without further purification. The 4,5-octanedione was prepared by permanganate oxidation from 4-octyne according to the method of Lee and Chang.[27] The nickel complexes were prepared by adding dropwise an excess
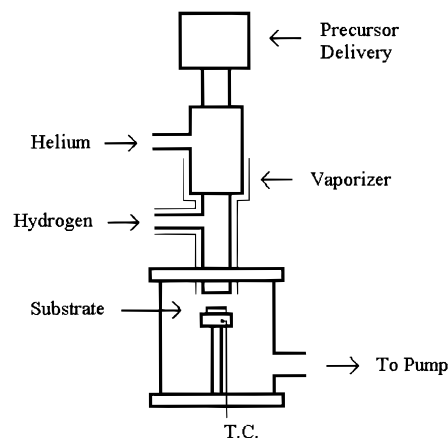
Figure 2. Diagram of the vertical, cold-walled MOCVD reactor.

of a concentrated aqueous solution of nickel acetate to a 50% ethanol/water solution of ligand. The complexes precipitated out immediately. The solutions were then refluxed for 2 h, cooled in ice, filtered, washed with cold water, and then dried under vacuum. ^{1}H NMR and IR spectroscopy confirmed the products, with yields ranging from 60 to 90%.

General. ^{1}H NMR spectra were recorded on a Varian Gemini-300 (300 MHz) spectrometer. Infrared spectra of the complexes (KBr pellets) were recorded on a Perkin-Elmer 983 spectrophotometer. Electronic spectra were recorded on a Cary 14 spectrophotometer by On-Line Instrument Systems, Inc. Spectra of the compounds were recorded as evaporated films (~0.2 mm thick) and in chloroform solution (~3 × 10^{-4} M). Thermogravimetric analysis was performed under nitrogen at atmospheric pressure and at a pressure of 15 mbar using a DuPont 951 TGA. Sample size was ~7 mg. Differential thermal analysis was performed under nitrogen at ambient pressure using a DuPont 1600 DTA. The temperature range of TGA/DTA was 20−600 °C with a ramp of 10 °C/min. MOCVD was performed on an in-house vertical reactor utilizing a flash evaporator (Figure 2). The flash evaporator consists of a device which continuously delivers precursor at a regular rate into the heated vaporizer, while the bulk supply is kept away from the heat. This is well-suited for temperature-critical precursors. Films were grown on single crystalline silicon (100) substrates, heated resistively. Substrates were cleaned with dilute nitric acid, rinsed with distilled water, and swabbed with acetone prior to use. Precursor mass flow in the reactor was evaluated by depositing precursor on a room temperature substrate holder (3 cm diameter) covered with a piece of tared aluminum foil. Reactor conditions which were held constant throughout the experiments were the evaporation temperature (200 °C), helium carrier gas flow rate (66 sccm), total pressure (30 mbar), and precursor delivery time into the flash evaporator (20 min). The thickness of the films was measured on a Tencor Alpha-Step 200 profilometer. Each film was measured five times in various locations, and the results were averaged. Typical growth rates were in the 400 Å/min range. X-ray diffraction data were recorded on a Siemens D-5000 diffractometer with the Cu anode in the θ-2θ mode. Atomic force microscopy (AFM) was conducted on a Denver Instruments AFM series Dimension 3000. The surface

(16) Carlton, H.; Oxle, J. *A.I.Ch.E.* **1967**, *13*, 86.

(17) Stauf, G.; Driscoll, D.; Dowben, P.; Barfuss, S.; Grade, M. *Thin Solid Films* **1987**, *153*, 421.

(18) Kaesz, H.; Williams, R.; Hicks, R.; Chen, Y.; Xue, Z.; Xu, D.; Shuh, D.; Thridandam, H. *Mat. Res. Soc. Symp. Proc.* **1989**, *131*, 395.

(19) Marboe, E. U.S. Pat 2,430,520; 1947.

(20) van Hemert, R.; Spenlove, L.; Sievers, R. *J. Electrochem. Soc.* **1965**, *112*, 1123.

(21) Kodas, T.; Hampden-Smith, M. *The Chemistry of Metal CVD*; VCH Publishers: New York, 1994.

(22) Schrauzer, G. *Angew. Chem. Int. Ed.* **1976**, *15*, 417.

(23) Thomas, T.; Underhill, A. *Chem. Soc. Rev.* **1972**, *1*, 99.

(24) Becht, M.; Gallus, J.; Hunziker, M.; Atamny, F.; Dahmen, K. H. *J. Phys. IV* **1995**, *5*, 465.

(25) Becht, M.; Atamny, F.; Baiker, A.; Dahmen, K. *Surface Sci.* **1997**, *371*, 399.

(26) Hach, C.; Banks, C.; Diehl, H. *Org. Synth.* **1952**, *32*, 35.

(27) Lee, D.; Chang, S. *Synthesis* **1978**, 462.

Table 1. Thermogravimetric Analysis Results

	ambient pressure			reduced pressure (15 mbar)		
compound	onset (°C)	T_{dec} (°C)	% remaining[a]	onset (°C)	T_{dec} (°C)	% remaining[a]
Ni(dpg)$_2$	205	255	81	120		4
Ni(deg)$_2$	186	241	80	130		0
Ni(g)$_2$	161	169	95	150	269[b]	67
Ni(meg)$_2$	196	251	84	150		0
Ni(dmg)$_2$	254	281	96	204	303	25
Ni(dbg)$_2$	301	322	70	280	340	63
Ni(nox)$_2$	257	263	98	257	263	98

[a] Percent remaining just prior to decomposition. [b] Final decomposition temperature for Ni(g)$_2$.
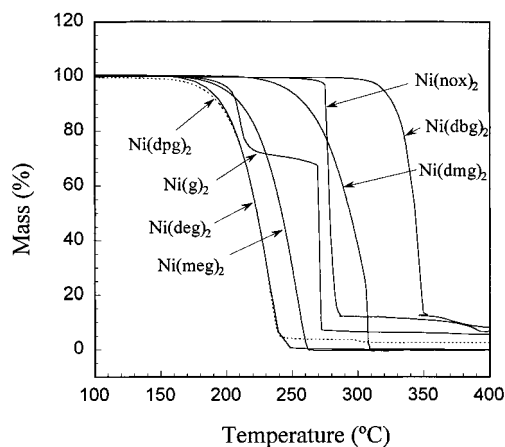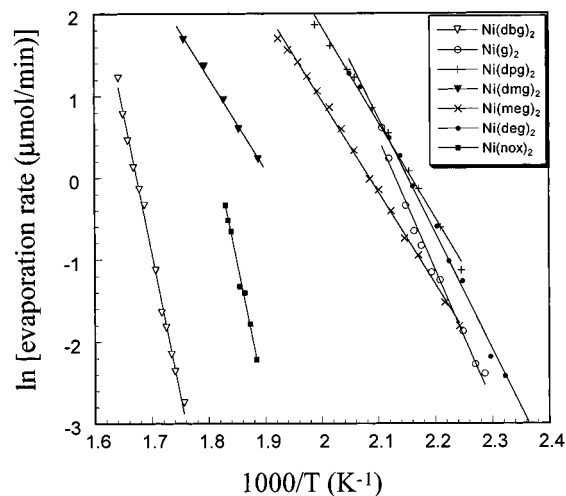
area of selected films was determined by tracing the substrate on a piece of weighing paper. The trace was then cut out and weighed and the weight was compared to the mass of a known area of weighing paper. X-ray photoelectron spectra (XPS) of the films were recorded on a Perkin-Elmer Phi-5100 system with a Mg anode at a take-off angle of 45°. Ar$^+$ sputtering with 4.5 kV acceleration energy was used for removing surface contamination and for depth analysis. Quantitation was based on peak area with an integrated baseline.

Crystal Structure Determination for Bis(4,5-octanedionedioximato)nickel(II), Ni(dpg)$_2$. The single crystal was obtained by slow evaporation of an ethanol solution. $C_{16}H_{30}N_4O_4Ni$, $M_r = 401.15$, monoclinic, $C2/c$, $a = 17.5190(3)$ Å, $b = 15.9509(2)$ Å, $c = 15.8964(2)$ Å, $\beta = 118.648(1)°$, $V = 3898.35(10)$ Å^3, $Z = 8$, $D_{calc} = 1.367$ g cm^{-3}. Data were collected at 173 K on a Siemens SMART PLATFORM equipped with a CCD area detector and a graphite monochromator utilizing Mo Kα radiation ($\lambda = 0.71073$ Å). Cell parameters were refined using 8192 reflections. A hemisphere of data (1321 frames) was collected using the w-scan method (0.3° frame width). The first 50 frames were remeasured at the end of data collection to monitor instrument and crystal stability (maximum correction on I was <1%). Integration absorption corrections were applied on the basis of indexed measured crystal faces. The structure was solved by the direct methods in *SHELXTL5*[28] and refined using full matrix least squares. The non-H atoms were treated anisotropically, whereas the hydrogen atoms were refined with isotropic thermal parameters and without any constraints. A total of 348 parameters were refined in the final cycle of refinement using 3902 reflections with $I > 2\sigma(I)$ to yield R_1 and wR_2 of 3.39% and 7.57%, respectively. Refinement was done using F^2.

Results and Discussion

All of the compounds synthesized are known from the literature.[29−31] Characterization was by IR and ^{1}H NMR, and results were in accord with the expected products and earlier literature reports.[32−37,57,58] Details of these results are provided as Supporting Information.

Thermal Analysis. Table 1 shows the thermal behavior of the compounds under ambient and reduced pressure as determined by TGA/DTA. Figure 3 shows the thermograms for reduced pressure. At ambient pressure none of the compounds sublimed to any great

(28) Sheldrick, G. *SHELXTL5*; Siemens Analytical Instrumentation: Madison, WI, 1995.
(29) Banks, C. *Rec. Chem. Progr.* **1964**, *25*, 85−104.
(30) Ferraris, G.; Viterbo, D. *Acta Cryst., Sect. B* **1969**, *25*, 2066.
(31) Banks, C.; Barnum, D. *J. Amer. Chem. Soc.* **1958**, *80*, 3579.
(32) Rundle, R.; Parasol, M. *J. Chem. Phys.* **1952**, *20*, 1487.
(33) Blinc, R.; Hadzi, D. *J. Chem. Soc.* **1958**, 4536.
(34) Burger, K.; Ruff, I.; Ruff, F. *J. Inorg. Nucl. Chem.* **1964**, *27*, 179.
(35) Caton, J.; Banks, C. *Inorg. Chem.* **1967**, *6*, 1670.
(36) Orel, B.; Penko, M.; Hadzi, D. *Spectrochim. Acta* **1980**, *36A*, 859.
(37) Bowers, M.; Hill, C. *Inorg. Chim. Acta* **1983**, *72*, 149.

Figure 3. Thermograms for the compounds taken at 15 mbar.

Figure 4. Arrhenius plots of the evaporation rates for the compounds at 15 mbar.

extent, for no endothermic peaks were discernable in the DTA. In every case, at the decomposition temperature there was a sudden discontinuous decrease in the mass, which corresponded with a large exothermic peak in the DTA. Examination of the TGA apparatus revealed blackened bits of decomposed compound which were thrown from the sample boat during the process. Under a reduced pressure of 15 mbar, all the compounds sublimed, with Ni(nox)$_2$ decomposing shortly after onset. Of the compounds studied, only Ni(deg)$_2$ and Ni(meg)$_2$ sublimed quantitatively. Ni(dpg)$_2$ left 4% residue, and Ni(dmg)$_2$ and Ni(dbg)$_2$ decomposed at 303 and 340 °C, respectively, as evidenced by the discontinuities in their plots.

Derivatives with respect to time of the mass change of the compounds were calculated to yield evaporation rates at reduced pressure. These rates were normalized by converting to μmol/min, and Arrhenius plots were constructed (Figure 4). The Clausius−Clapeyron equation relates the enthalpy of sublimation to the variation of vapor pressure of an ideal gas with temperature:[38]

$$\Delta H_{sub} = -R\left(\frac{d \ln P}{d \, 1/T}\right)$$

(38) Castellan, G. *Physical Chemistry*, 2nd ed., Addison-Wesley: Menlo Park, CA, 1983.

Table 2. Arrhenius Plot Data for the Compounds at 15 mbar

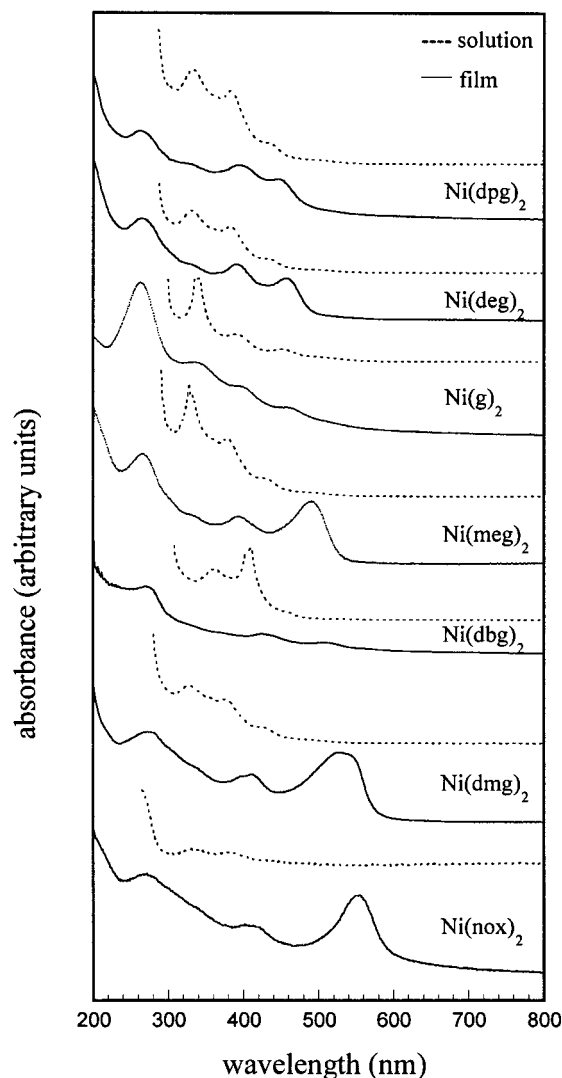| compound	line equation	R fit	ΔH_{vap} (kJ/mol)
Ni(dpg)$_2$	$y = 26.029 - 12.067x$	0.99448	100.3
Ni(deg)$_2$	$y = 27.773 - 12.905x$	0.99206	107.2
Ni(g)$_2$	$y = 32.833 - 15.435x$	0.98092	128.3
Ni(meg)$_2$	$y = 25.062 - 12.041x$	0.99637	100.1
Ni(dmg)$_2$	$y = 22.711 - 11.923x$	0.99677	99.12
Ni(dbg)$_2$	$y = 61.079 - 36.494x$	0.99154	303.4
Ni(nox)$_2$	$y = 62.334 - 34.243x$	0.99103	284.6

As the Langmuir equation[39] shows the vapor pressure of a solid to vary linearly with its evaporation rate, the enthalpy of sublimation measured at 15 mbar was calculated by multiplying the slopes of these plots by $-R$. The equations for the lines, their linear fit, and the calculated enthalpy values are shown in Table 2.

From the thermograms and Arrhenius plots, the ranking of volatilities is therefore:

$$Ni(dpg)_2 > Ni(deg)_2 > Ni(g)_2 \geq Ni(meg)_2 >$$
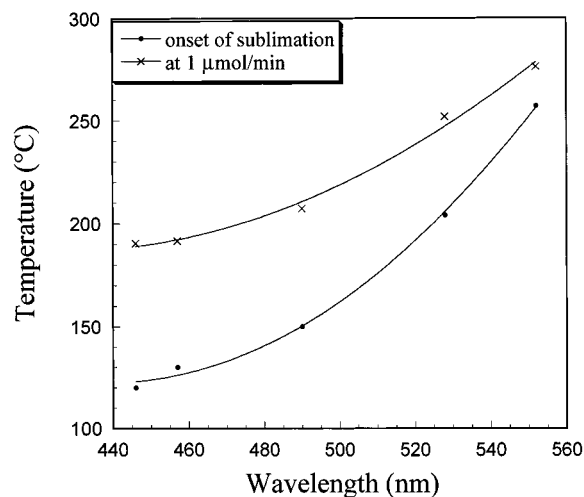$$Ni(dmg)_2 > Ni(nox)_2 > Ni(dbg)_2$$
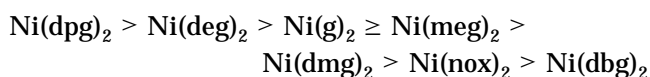
The volatility of the compounds is determined by a number of factors, including the presence or absence of van der Waals forces between molecules, the packing force of the molecule in the crystal, and the Lewis acidity of the metal center. Generally, the capacity of the metal center to interact intermolecularly is governed by electron-withdrawing ligands, the number of d electrons per metal ion, and the steric hindrance of the ligand.[40] As the calculated enthalpies of sublimation related poorly to the molecular weights of the compounds, it appears that the steric hindrance of the ligand and van der Waals interactions are not directly controlling the volatility. To help clarify this, electronic spectra were obtained for each in chloroform solution and as evaporated films on quartz substrates (Figure 5). For the films, three major bands were observed. The bands around 280 nm are assigned to the $\pi-\pi^*$ transition of the ligand, and the bands around 400 nm are assigned to the metal to ligand charge transfer transition.[41] The band in the visible region varies and is assigned to the $d_{z^2}-p_z$ transition from intermolecular metal–metal interactions. The position of this band, which is shifted to much higher energy in solution, has been successfully used to predict metal–metal distances.[23]

Figure 6 shows a plot of the sublimation onset temperature and the temperature at which each complex has an evaporation rate of 1 μmol/min, each as a function of the wavelength of the visible band. Clearly, for the alkyl substituted complexes, the higher the energy of the band, the greater the volatility. The convergence of the two plots is likely a consequence of the varying molecular weights of the complexes. Not included in this series are Ni(g)$_2$ and Ni(dbg)$_2$, which are anomalous. For Ni(dbg)$_2$, this may be due to a differing spectrum, but also to the electron-withdrawing

(39) Langmuir, I. *Phys. Rev. (second series)* **1913**, *2*, 329.
(40) Endres, H.; Keller, H.; Lehmann, R.; Poveda, A.; Rupp, H.; Sand, H. *Z. Naturforsch* **1977**, *32*, 516.
(41) Ohashi, Y.; Hanazaki, I.; Nagakura, S. *Inorg. Chem.* **1970**, *9*, 1970.

Figure 5. Electronic spectra of the compounds as evaporated films ($\sim$0.2 mm thick), and in chloroform solution ($\sim$3 $\times$ 10^{-4} M).

Figure 6. Sublimation temperatures as a function of the wavelength of the visible region band for (left to right) Ni(dpg)$_2$, Ni(deg)$_2$, Ni(meg)$_2$, Ni(dmg)$_2$, Ni(nox)$_2$.

effect and π stacking of the phenyl groups, both of which increase intermolecular attraction. Ni(g)$_2$ has an unusual crystal structure, considering the low bulk of the

ligand,[42] and the hydrogen substituents allow the possibility for additional van der Waals forces (a close approach of 2.34 Å occurs between a =CH proton and the oxygen of a neighboring molecule).

For Ni(dmg)$_2$ and Ni(nox)$_2$, the presence of interactions between metal atoms occurs as the planar molecules stack 90° staggered in a columnar structure forming metal atom chains containing delocalized electrons. Both belonging to the orthorhombic crystal system, Ni(dmg)$_2$ and Ni(nox)$_2$ have metal−metal (M−M) distances of 3.245 Å and 3.237 Å, respectively.[31,43]

Ni(meg)$_2$ reportedly has α and β crystal forms,[44,45] the former monoclinic (eclipsed packing), with M−M = 4.75 Å,[46] and the latter orthorhombic (staggered packing), with M−M = 3.44 Å.[45,47] The preparation determines which modification is obtained, with fast precipitation from reactants favoring the orange β phase and slow recrystallization from chloroform favoring the red α phase. While the α form is thermodynamically more stable, the β form is kinetically favored, and heating will not convert it to the α form due to the improbability of eclipsed molecules rotating in the solid state to become staggered. On the basis of our preparation, the X-ray diffraction pattern of the film,[45] and the UV spectrum,[41] we conclude that it is β-Ni(meg)$_2$ with which we have dealt. Its volatility is in the range we would expect from the position of its visible band and the closer M−M distance, and since the energy barrier to the α-phase cannot be surmounted by heating, it sublimes as the β modification.

The energy of the visible band for the other compounds suggests that d_{z^2} and p_z electrons are more localized. Apparently a columnar structure with staggered packing is precluded if the substituents are large, as in Ni(dpg)$_2$, or small, as in Ni(g)$_2$.[23] In the monoclinic form the molecules are eclipsed and shift as they pack, with metal−metal interaction being very weak. For these the position of the visible band in the solid-state spectra approaches the position observed in the solution spectra, where there can be no M−M interaction at all. Banks has shown that the solubility of *vic*-dioximates is related to metal−metal distance, with shorter distances decreasing their solubility in organic solvents.[31] Lengthening of metal−metal distance has also been observed at low pressure and high temperature,[48,49] so it seems reasonable that the longer distances will lead to greater volatility. From the energy of the visible band we predicted that M−M for Ni(dpg)$_2$ and Ni(deg)$_2$ would be 4.35 and 4.04 Å, respectively. To test this prediction, the X-ray crystal structure of Ni(dpg)$_2$ was determined (discussed in the next section). It was found that Ni(dpg)$_2$, in fact, has a short Ni−Ni distance of 3.2044(5) Å within a pair of stacking molecules and a long distance of 5.7964(5) Å between a pair (see packing diagram, Figure 8). Although the short distance is even closer than in Ni(nox)$_2$, the shifting must prevent
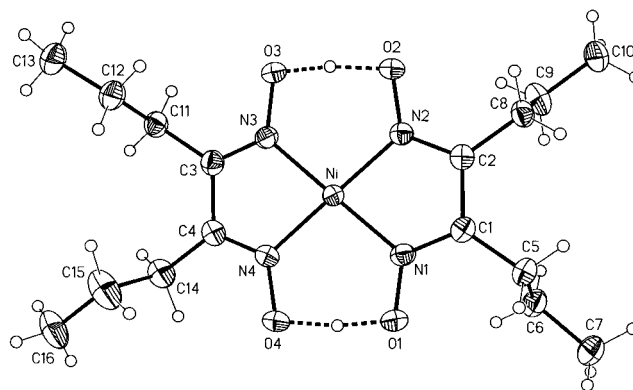

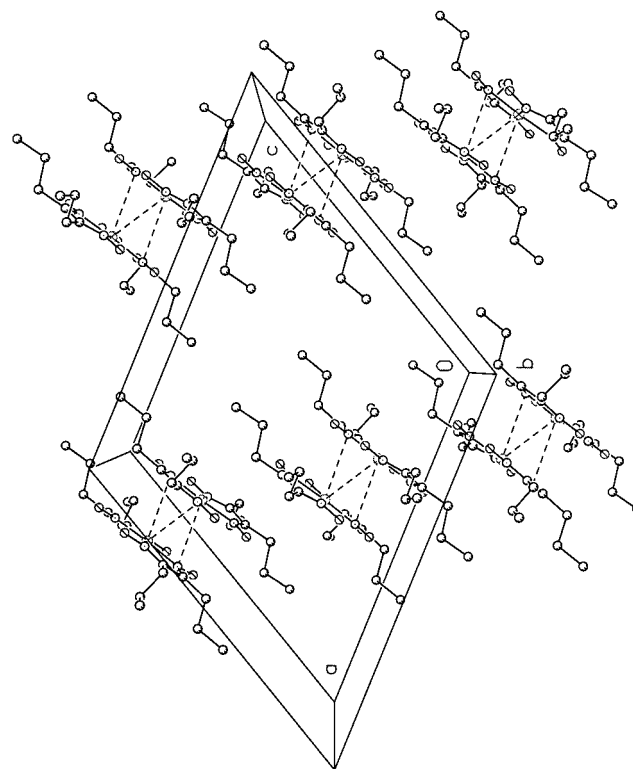**Figure 7.** Crystal structure of Ni(dpg)$_2$.

Figure 8. Packing diagram for Ni(dpg)$_2$, viewed along *b*. Parallel dashed lines within a pair represent close contacts of 3.312(2) Å between Ni and N2, while the transverse dashed line represents Ni−Ni contacts of 3.2044(5) Å.

effective overlap of the adjacent d_{z^2} and p_z orbitals, lest the volatility would suffer. The average of the short and long distance, however, is a close approximation to that predicted from the electronic spectrum. Higher volatility could also be due to the fact that Ni(dpg)$_2$ has half the number of close nickel atoms as that of Ni(dmg)$_2$ and Ni(nox)$_2$. The next nearest intermolecular contact is between Ni and N, thus van der Waals forces are minimal. The sheetlike packing of the molecules also helps explain the lower melting point of Ni(dpg)$_2$. We therefore conclude, that, for the alkyl-substituted series, metal−metal interactions are most important for the complexes with orthorhombic systems. By increasing the bulk of the ligand, monoclinic packing occurs, which results in more localized electrons and thus metal−metal interactions that are limited to a degree approaching that of solution, increasing the volatility. These interactions are reflected in the electronic spectra

(42) Calleri, M.; Ferraris, G.; Viterbo, D. *Acta Crystallogr.* **1967**, *22*, 468.

(43) Godycki, L.; Rundle, R. *Acta Crystallogr.* **1953**, *6*, 487.

(44) Anex, B.; Krist, F. *J. Am. Chem. Soc.* **1967**, *89*, 6114.

(45) Egneus, B. *Anal. Chim. Acta* **1969**, *48*, 291.

(46) Bowers, R.; Banks, C.; Jacobson, R. *Acta Crystallogr., Sect. B* **1972**, *28*, 2318.

(47) Sharpe, A.; Wakefield, D. *J. Chem. Soc.* **1957**, 281.

(48) Shirotani, I.; Suzuki, T. *Solid State Commun.* **1986**, *59*, 533.

(49) Gliemann, G.; Yersin, H. *Struct. Bonding* **1985**, *62*, 87.

Table 3. Selected Bond Angles and Lengths for Ni(dpg)$_2$

bond	angle (deg)	bond	length (Å)
N1−Ni−N2	82.74(7)	Ni−N1	1.863(2)
N1−Ni−N3	176.47(7)	Ni−N2	1.865(2)
N2−Ni−N3	97.19(7)	Ni−N3	1.868(2)
N1−Ni−N4	97.45(7)	Ni−N4	1.870(2)
N2−Ni−N4	175.84(7)	O1−N1	1.339(2)
N3−Ni−N4	82.36(7)	O1−H1	1.17(4)
N1−O1−H1	103(2)	N1−C1	1.302(3)
C1−N1−O1	120.5(2)	C1−C2	1.471(3)
C1−N1−Ni	116.11(14)	C1−C5	1.493(3)
O1−N1−Ni	123.38(13)	O2−N2	1.344(2)
O1−N1−Ni	123.38(13)	O2−H3	1.28(4)
N1−C1−C2	112.6(2)	N2−C2	1.303(2)
N1−C1−C5	121.9(2)	C2−C8	1.495(3)
C2−C1−C5	125.5(2)	O3−N3	1.350(2)
N2−O2−H3	102(2)	O3−H3	1.18(4)
C2−N2−O2	120.0(2)	N3−C3	1.294(3)
C2−N2−Ni	116.26(13)	C3−C4	1.475(3)
O2−N2−Ni	123.72(12)	C3−C11	1.496(3)
N2−C2−C1	112.2(2)	O4−N4	1.354(2)
C1−C2−C8	125.1(2)	O4−H1	1.29(4)
N3−O3−H3	102(2)	N4−C4	1.295(3)
C3−N3−O3	112.4(2)	C4−C14	1.504(3)
C4−C3−C11	124.4(2))		
N4−O4−H1	101(2)		
C4−N4−O4	116.16(14)		
O4−N4−Ni	123.64(13)		
N4−C4−C3	112.3(2)		
N4−C4−C14	123.3(2)		
C3−C4−C14	124.4(2)		

Table 4. Crystal Data and Structure Refinement for Ni(dpg)$_2$

empirical formula	$C_{16}H_{30}N_4O_4Ni$
formula weight	401.15
temperature	173(2) K
wavelength	0.71073 Å
crystal system	monoclinic
space group	$C2/c$
unit cell dimensions	$a = 17.5190(3)$ Å, $\alpha = 90°$
	$b = 15.9509(2)$ Å, $\beta = 118.648(1)°$
	$c = 15.8964(2)$ Å, $\gamma = 90°$
volume, Z	3898.35(10) Å^3, 8
density (calculated)	1.367 Mg/m^3
absorption coefficient	1.022 mm^{-1}
F(000)	1712
crystal size	$0.21 \times 0.18 \times 0.09$ mm
θ range for data collection	1.84 to 27.50°
limiting indices	$-22 \leq h \leq 19$, $-20 \leq k \leq 11$,
	$-20 \leq l \leq 19$
reflections collected	25561
independent reflections	4465 [R(int) = 0.0339]
absorption correction	integration, based on crystal faces
max. and min. transmission	0.9174 and 0.8015
refinement method	full-matrix least squares on F^2
data/restraints/parameters	4465/0/348
goodness-of-fit on F^2	1.092
final R indices [$I > 2$ sigma(I)]	$R_1 = 0.0339$, $wR_2 = 0.0757$ [3902]
R indices (all data)	$R_1 = 0.0423$, $wR_2 = 0.0820$
extinction coefficient	0.00011(4)
largest diff peak and hole	0.874 and −0.276 e Å^{-3}

and correlate with the volatilities for these compounds quite well.

Crystal Structure of Ni(dpg)$_2$. The structure of the molecule is shown in Figure 7. The nickel atom has a distorted square planar coordination geometry and lies at a distance of 0.062(1) Å from the coordination plane. The O−O distance is similar to that found for other nickel *vic*-dioximes,[42,43,46] with O3−O2 distance of 2.448(2) Å. The complex contains an essentially symmetric hydrogen bridge, with O3−H3 of 1.18(4) Å and O2−H3 of 1.28(4) Å. Other selected intermolecular distances and angles are shown in Table 3. The complex packs in pairs related by the *c*-glide symmetry. Short intrapair distances are observed between Ni and N2 [Ni−N2 is 3.312(2) Å and the angle N2−Ni−N2 (1 − *x*, *y*, 2.5 − *z*) is 109.32(5)°]. The packing diagram (Figure 8), viewed along *b*, shows that pairs of molecules pack in a fashion close to columns, but do not interlock. The coordination planes are parallel, but each is slid from its neighbor by approximately 4 Å. Inside a pair (symmetry 1 − *x*, *y*, 2.5 − *z*) the Ni−Ni distance is 3.2044(5) Å and for adjacent Ni atoms in different pairs (symmetry 0.5 − *x*, 0.5 − *y*, 2 − *z*) the spacing is 5.7964(5) Å. Table 4 summarizes the crystal data for Ni(dpg)$_2$.

Film Growth Behavior Using Ni(deg)$_2$ as MOCVD Precursor. Because of its favorable volatility and thermal stability and ease of synthesis, it was decided that Ni(deg)$_2$ was the best candidate for the MOCVD experiments. Using this precursor, we were successful in obtaining nickel films. First, deposition was conducted at various substrate temperatures using helium carrier gas alone (66 sccm) or with 90 sccm additional hydrogen reaction gas (Figure 9a). The delivery rate of precursor into the flash evaporator was ~8.7 μmol/min (60 mg added over 20 min). At 400 °C, use of added hydrogen increased the growth rate as opposed to use of helium alone. However, at lower substrate temper-

atures, growth was less in hydrogen, and at 350 °C, modest growth occurred with helium where no growth occurred using hydrogen. This suggests that between about 360 and 380 °C hydrogen may compete with precursor for surface sites, while from 390 to 400 °C, it improves the precursor decomposition. Films grown at temperatures over 400 °C using hydrogen were blackened, powdery, and nonadherent (suggestive of gas phase nucleation) and are therefore not shown in Figure 9a. As can be seen, the range of film growth was more extended for helium-grown films, which were overall smoother and shinier in appearance, as opposed to the dull gray color produced with added hydrogen. Figure 9a shows that the growth of films in hydrogen is kinetically controlled over the entire range with the slope of the plot indicating a "pseudo" activation energy of approximately 140 kJ/mol. Two regimes can be distinguished for the helium-grown films: between 350 and 450 °C the growth is kinetically controlled with an activation energy of about 40 kJ/mol, while above 450 °C the growth is controlled by mass flow of precursor to the substrate. These values are comparable to those found in MOCVD of other metals using β-diketones; however, in most cases, the apparent activation energy was smaller when hydrogen reaction gas was used.[21,50−52]

The variation of hydrogen flow rate was next investigated at a substrate temperature of 400 °C and a precursor delivery rate of ~8.7 μmol/min. As can be seen from Figure 9b, increasing the H$_2$ flow rate from 0 to 100 sccm had a pronounced effect on the growth rate, with thicker films resulting from higher flow rates. This plot shows that the maximum growth rate occurs with flow rates of about 60 sccm. The appearance of the films

(50) Fine, S.; Dyer, P.; Norman, J.; Mratore, B.; Iampeitro, R. *Mater. Res. Soc. Symp. Proc.* **1990**, *204*, 415.

(51) Jain, A.; Chin, K.; Hampden-Smith, M.; Kodas, T.; Paffett, M.; Farr, J. *J. Electrochem. Soc.* **1993**, *140*, 1434.

(52) Auvert, G. *Appl. Surf. Sci.* **1998**, *43*, 47.
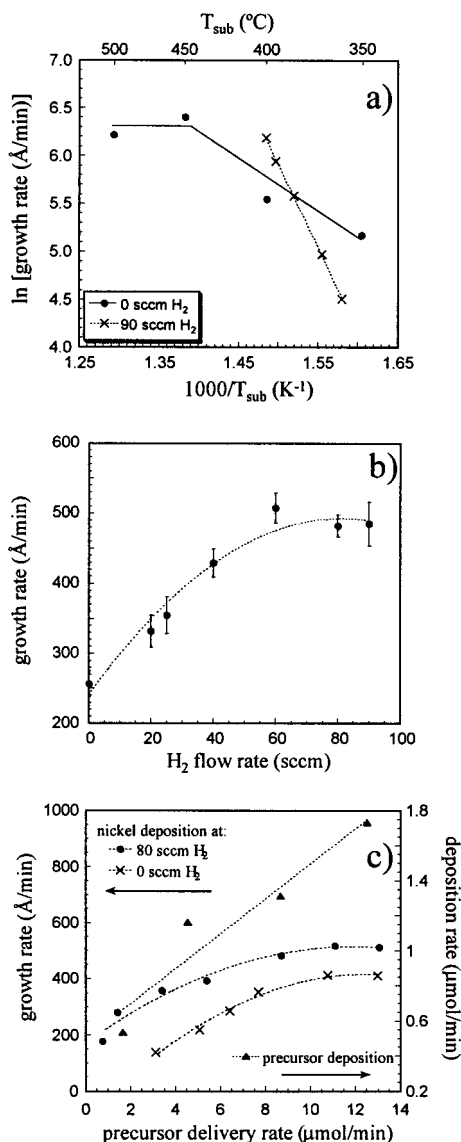
Figure 9. (a) Arrhenius plot for the growth rate as a function of substrate temperature at 0 and 90 sccm of H_2 with precursor delivery of 8.7 μmol/min. (b) Growth rate as a function of H_2 flow, with delivery of 8.7 μmol/min and T_{sub} of 400 °C. (c) Growth rate of nickel at 0 and 80 sccm of H_2 flow (T_{sub} = 400 °C) and deposition rate of Ni(deg)$_2$ as functions of precursor delivery rate.

for this series progressively changed from smooth and mirrorlike at the low H_2 flow rates to duller and grayer at the higher rates. The roughness of these films also increased, as evidenced by greater deviations in the thickness measurements of films grown at 90 and 100 sccm of H_2.

Figure 9c shows the effect of delivery rate of precursor on growth rate using helium carrier gas or helium with an added 80 sccm of hydrogen at 400 °C. Also plotted is the deposition rate of precursor on a room temperature substrate holder. Again, films grown in hydrogen had consistently higher growth rates than He-grown films. In both cases, the growth rate became constant at a precursor delivery rate of about 9 μmol/min. This could be due to the mass flow of precursor becoming constant due to "overloading" of the flash evaporator; however, the deposition experiments prove that mass flow is still increasing past this delivery rate, so the
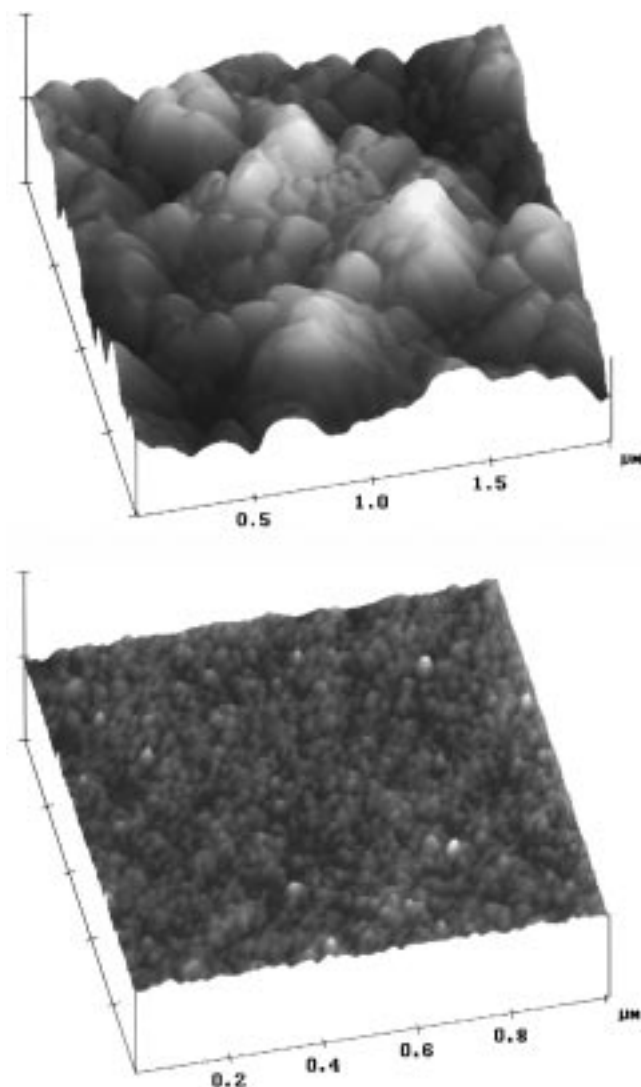
constancy in growth rate here must be due to surface kinetics. For the He-grown films, the plot resembles that theoretically obtained from a unimolecular Langmuir−Hinshelwood (L−H) adsorption mechanism.[53] At lower deliveries, the surface still contains empty sites at which precursor molecules may adsorb, so the growth here depends on the delivery, resulting in first-order kinetics. At higher deliveries, the sites are all occupied, such that growth is independent of precursor delivery, and the kinetics are zero-order. For H_2-grown films, plots in Figure 9b,c indicate a Rideal−Eley mechanism,[54] in which there is no competition for surface sites by precursor and hydrogen. The two reactants must therefore occupy the same site prior to decomposition. This mechanism makes sense, for according to the L−H model, the precursor ideally has the same number of adsorption sites whether or not hydrogen is used and saturation occurs at the same delivery rate for either condition.

Morphology. The crystallinity of selected films was determined by XRD. All of the films showed some degree of crystallinity with peaks corresponding to the (111), (200), and (220) reflections for polycrystalline nickel. The intensities were proportional to those of the JCPDS file. The full-widths at half-height for the (111) reflections revealed all the H_2-grown films to have similar crystallinity. These measured widths were about four times larger for the helium-grown films, a testament to the lower crystallinity. For the hydrogen-grown films, the existence of nickel hydride phases is not yet proven.[55,56]

AFM pictures (Figure 10a,b) were obtained of a film grown with helium only and of a film grown with 80 sccm of added hydrogen. Both films were approximately 5700 Å thick. Table 5 summarizes the results. The pictures show the drastic difference in the two types of films. The He-grown film is remarkably flat for this thickness, with very uniform grain sizes. On the other hand, the film grown in hydrogen has a wide range of grain sizes, with larger grains likely giving rise to the observed greater crystallinity and roughness. Also shown are large voids between grains.

To determine if the greater thickness of the hydrogen-grown films was really a consequence of more efficient precursor decomposition or merely a result of lower film density, the density of representative samples was measured. This entailed destroying the films to record their mass by difference. Neglecting coverage on the sides of the substrate, the volume of the film was calculated knowing its thickness and surface area. For a film grown at 40 sccm of hydrogen, the density was found to be only 4.3 g/cm^3, while for a helium-grown film, the density was 7.3 g/cm^3, closer to the bulk value for nickel, 8.9 g/cm^3. This is supported by the AFM pictures which show the H_2-grown films to be more porous. We therefore conclude that the greater growth

(53) Langmuir, I. *J. Am. Chem. Soc.* **1916**, *38*, 1145.
(54) Rideal, E. *Proc. Cambr. Philos. Soc.* **1939**, *35*, 130.
(55) Greenwood, N.; Earnshaw, A. *Chemistry of the Elements*; Pergamon Press: Oxford, 1984.
(56) Cotton, F.; Wilkonson, G.; *Advanced Inorganic Chemistry*, 3rd ed., Interscience Publishers: New York, 1972.
(57) Voter, R.; Banks, C.; Fassel, V.; Kehres, P. *Anal. Chem.* **1951**, *23*, 1730.
(58) Panja, P.; Bala, S.; Pal, C.; Ghosh, P. *J. Mol. Struct.* **1991**, *249*, 277.

Table 6. XPS Results

H$_2$ flow rate (sccm)	40	0
thickness (Å)	8583	5130
composition (atom %)		
Surface		
Ni	14.03	18.96
C	62.67	44.19
O	23.30	36.86
150 Å sputtered		
Ni	69.44	83.08
C	30.56	13.81
O	<1[a]	3.10
300 Å sputtered		
Ni	74.32	>99
C	25.68	<1[a]
O	<1[a]	<1[a]

[a] XPS signals unresolvable from baseline noise.

revealed little difference in the final analysis, indicating the impurities were deeper still. These results are rather surprising. In most metal CVD processes, hydrogen was found to be useful for reducing the carbon contamination.[16–18] As discussed in the previous sections, the introduction of hydrogen leads to a reaction pathway (Rideal–Eley mechanism) which results in a higher growth rate. The greater porosity and larger grain boundaries could be responsible for some impurity retention, but these results, taken with the lower film density/higher porosity and narrow growth temperature range, show that hydrogen leads to poor precursor decomposition and resulting poor film quality.

Conclusions. It has been shown that by increasing the bulk of the dioxime ligand, the resulting nickel complexes have net metal–metal distances approaching that of solution, with the volatilities correlating well with the distances inferred from their solid-state electronic spectra. Compared to Ni(dmg)$_2$, and in some respects other nickel precursors, Ni(deg)$_2$ has many more desirable features of an ideal precursor: it is quite volatile and films could be obtained at higher pressures and lower evaporation temperatures; it is thermally stable over a wide temperature range; it gives clean decomposition and high growth rates at relatively low substrate temperatures without the necessity of reaction gas; it is nontoxic, air-stable, cheap, and easy to synthesize.

Supporting Information Available: IR and 1H NMR characterization of the compounds, and details of the structure determination for Ni(dpg)$_2$, including all calculated atomic coordinates and equivalent isotropic displacement parameters; bond lengths and angles including nonessential atoms; anisotropic displacement parameters; hydrogen coordinates, isotropic displacement parameters, hydrogen bonding parameters; packing diagrams (15 pages); and observed and calculated structure factors (11 pages). Ordering information is given on any current masthead page.

CM980286V

Figure 10. AFM picture of (a) 5630 Å nickel film grown using 66 sccm of He carrier gas and 80 sccm of H$_2$ reaction gas, with T_{sub} = 400 °C. The x and y axes are 0.5 μm/div; the z axis is 500 nm/div. (b) 5730 Å nickel film grown using 66 sccm of He carrier gas alone, with T_{sub} = 400 °C. The x and y axes are 0.2 μm/div; the z axis is 30 nm/div.

Table 5. AFM Results

	80 sccm % H$_2$	0 sccm % H$_2$
thickness (Å)	5633	5728
surface area of 1 μm section (μm)	1.85	1.009
roughness, R_a	98.9	0.6
average grain size (nm)	110	16

rates observed for H$_2$-grown films are due to higher porosity, not to more efficient decomposition.

Film Composition. Regarding the efficiency of decomposition of precursor for the two reactor conditions and the possibility of decomposition by-products being incorporated in the film, XPS was performed on representative samples of films grown at 400 °C using 66 sccm of helium and helium with 40 sccm of added hydrogen. Table 6 summarizes the results. The results show that films grown in helium were essentially pure nickel, with some surface contamination. Films grown in the presence of hydrogen were contaminated within the film with carbon and oxygen as deep as 300 Å. Analyzing this film at take-off angles of 30° and 15°